



Interfacial electronic modulation of Ni₃S₂ nanosheet arrays decorated with Au nanoparticles boosts overall water splitting

Hui Liu^{a,c,*}, Jianing Cheng^{a,1}, Wenjun He^a, Ying Li^a, Jing Mao^b, Xuerong Zheng^{b,**}, Cong Chen^a, Chunxiang Cui^d, Qiuyan Hao^{a,**}

^a School of Materials Science and Engineering, Key Laboratory of Special Functional Materials for Ecological Environment and Information (Hebei University of Technology), Ministry of Education, Tianjin 300130, PR China

^b School of Materials Science and Engineering, Tianjin University, Tianjin Haihe Education Park, Tianjin 300072, PR China

^c Department of Physics and Astronomy, University of California, CA 92697, USA

^d Key Laboratory for New Type of Functional Materials in Hebei Province, School of Materials Science and Technology, Hebei University of Technology, No.5340, Xiping Road, Beichen District, Tianjin 300401, China

ARTICLE INFO

Keywords:

Heterostructure
Ni₃S₂
Bifunctional
Overall water splitting
Density functional theory

ABSTRACT

Rationally design and exploration of bifunctional electrocatalysts with excellent performance towards water splitting is significant for hydrogen energy economy. Herein, a novel Au/Ni₃S₂ heterostructure catalyst that was composed of self-supported Ni₃S₂ nanosheets decorated with Au nanoparticles on Ni foam was fabricated. The bifunctional catalyst exhibited excellent catalytic activities towards oxygen evolution reaction (230 mV @ 10 mA cm⁻²) and hydrogen evolution reaction (97 mV @ 10 mA cm⁻²) in 1 M KOH. The electrolytic tank using the bifunctional catalyst only required 1.52 V to deliver 10 mA cm⁻² and sustained for 60 h, outperforming most of advanced bifunctional catalysts. The X-ray absorption fine structure (XAFS) and density functional theory (DFT) calculations validated that the strong electronic coupling at the interface could modulate the electronic structure of Ni₃S₂, thereby optimizing the free energies of the adsorbed intermediates. This work provides an atomic-scale insight into the structure-properties relation of a promising heterostructure catalyst for water splitting.

1. Introduction

The excessive consumption of fossil energy has caused severe energy crisis and greenhouse effect, so it's extremely urgent to search for sustainable and cost-effective clean energy [1–4]. Owing to its high energy density (~ 282 kJ mol⁻¹), abundant reserves and carbon-free emission, hydrogen energy is regarded as one promising alternative to fossil energy [5–7]. Especially, electrochemical water splitting powered by renewable energy provides a reliable and environmental-friendly approach to hydrogen generation [8–10]. To facilitate the sluggish cathodic hydrogen evolution reaction (HER) as well as the anodic oxygen evolution reaction (OER) during water splitting, the utilization of electrocatalysts is inevitable. Until now, the most advanced catalysts for HER and OER are Pt-based materials and RuO₂/IrO₂, respectively [11, 12]. Despite the excellent catalytic activity, their scarcity and inferior

durability still enormously inhibit their large-scale industrialization [13]. Hence, the exploration of low-cost bifunctional electrocatalysts with high activity and long-term durability towards both HER and OER have become a hot spot in the field of water splitting.

In the past decades, a series of transition-metal compounds such as sulfides, selenides, phosphides and nitrides has attracted great attention due to their low cost and bifunctional activity for both HER and OER in alkaline solution [14–18]. Among them, Ni₃S₂ catalyst stands out because of its high conductivity and unique electronic structure, which is widely considered as a promising bifunctional electrocatalysts [19, 20]. However, the catalytic activity and stability of Ni₃S₂ catalyst towards both HER and OER in alkaline media is far from satisfactory in contrast to noble metal-based catalysts, which is attributed to their poorly intrinsic activity [21,22]. On one hand, for HER, many former studies suggested that the very weak adsorption of H intermediate on

* Corresponding author at: School of Materials Science and Engineering, Key Laboratory of Special Functional Materials for Ecological Environment and Information (Hebei University of Technology), Ministry of Education, Tianjin 300130, PR China.

** Corresponding authors.

E-mail addresses: liuhuihebut@163.com (H. Liu), xrzh@tju.edu.cn (X. Zheng), hutcu@hebut.edu.cn (C. Cui), hqy1218@163.com (Q. Hao).

¹ H. Liu and J. Cheng contributed equally to this work.

Ni_3S_2 surface led to its poor activity [23], and amounts of strategies such as doping [24], defect [25] and interface engineering [26] were successful in boosting the HER activity of Ni_3S_2 catalyst by optimizing the Gibbs free energy of H adsorption (ΔG_{H^+}). Nevertheless, recent studies revealed that the cleavage of O-H bond of H_2O on Ni_3S_2 catalyst in alkaline media may be the real rate-determining step during HER, leading to a sluggish kinetics [27]. On the other hand, for OER, some studies demonstrated that the surface of Ni_3S_2 would be partially transformed into nickel (oxy)hydroxides at a high redox potential during OER, implying the real catalytic species may be nickel (oxy)hydroxides rather than nickel sulfides [28]. Given that the poor conductivity and inferior intrinsic activities of nickel (oxy)hydroxides, it is easy to understand why Ni_3S_2 possesses a poor OER performance [29].

To simultaneously promote the HER and OER activities of the bifunctional catalysts, constructing heterostructure via hybridizing metal species with high conductivity has been demonstrated as an efficient means because of the following merits: (I) improving the conductivity of the catalysts [30]; (II) generating a local electric field at the interface of heterostructure that may promote the dissociation of H_2O on the active sites of the catalysts, which is beneficial for alkaline HER [31]; (III) regulating the electronic structure of the active sites that may optimize the adsorption free energies of the reaction intermediates during HER/OER process [23,32]. Considering that Au has many advantages such as good conductivity, outstanding oxidation resistance and high work function (5.1), we speculated that hybridizing Au with Ni_3S_2 ($\text{Au}/\text{Ni}_3\text{S}_2$) may not only increase the conductivity of the catalyst, but also cause a strong electronic interaction at their interface, which may boost both HER and OER performance of Ni_3S_2 catalyst. Here, we reported a novel $\text{Au}/\text{Ni}_3\text{S}_2$ heterostructure nanosheet arrays on Ni foam ($\text{Au}/\text{Ni}_3\text{S}_2/\text{Ni}$ foam) that was fabricated by two-step hydrothermal method and chemical reduction process. The heterostructure catalyst exhibited excellent bifunctional catalytic activity, only needing low overpotentials of 97 and 230 mV to drive the current density of 10 mA cm^{-2} for HER and OER in 1 M KOH, respectively. Additionally, an electrolytic tank using $\text{Au}/\text{Ni}_3\text{S}_2/\text{NF}$ as both cathode and anode only required a relatively low cell voltage of 1.52 V to reach the current density of 10 mA cm^{-2} , and sustained long-term stability for 60 h with negligible degradation. The advanced XAFS and DFT calculation suggested that the strong electronic coupling at the interface of Ni_3S_2 and Au could activate H_2O molecular and optimize H/O intermediates during HER and OER. This strategy through using Au to modulate the electronic structure of bifunctional electrocatalysts may not only be used to boost the catalytic performance of Ni_3S_2 , but to enhance other transition-metal sulfides, phosphides and beyond [14,33].

2. Experimental section

2.1. Materials

The pristine Ni Foam (NF) and Nafion (5 wt%) were obtained by Sigma-Aldrich. $\text{Ni}(\text{NO}_3)_2 \cdot 6\text{H}_2\text{O}$, NH_4F , urea, ethyl alcohol and HAuCl_4 were bought from Beijing Innochem. 2-mercaptoethanol, $\text{Na}_3\text{C}_6\text{H}_5\text{O} \cdot 5\text{H}_2\text{O}$ and NaBH_4 were purchased from Aladdin. Commercial Pt/C (20 wt%) and IrO_2 catalyst were purchased from Alfa Aesar. The pristine NF ($1 \times 3 \text{ cm}^2$) were ultrasonically immersed into HCl solution and alcohol to ensure the clean surface.

2.2. Synthesis of catalysts

2.2.1. Synthesis of $\text{Ni}(\text{OH})_2/\text{NF}$ catalysts

$\text{Ni}(\text{NO}_3)_2 \cdot 6\text{H}_2\text{O}$ (2 mmol), NH_4F (4 mmol), urea (10 mmol) were successively dissolved in 35 mL deionized water (DIW). Then the mixed solution and two pieces of NF were dispensed into autoclave and maintain at 120 °C for 6 h. After reaction, the obtained $\text{Ni}(\text{OH})_2/\text{NF}$ was washed and dried for further use.

2.2.2. Synthesis of $\text{Ni}_3\text{S}_2/\text{NF}$ catalysts

The synthesis of $\text{Ni}_3\text{S}_2/\text{NF}$ nanosheets is as following: 2-mercaptoethanol (2.5 mL) and ethanol (25 mL) were dispersed in the autoclave. Then, a piece of $\text{Ni}(\text{OH})_2/\text{NF}$ was placed into sealed autoclave and heated at 150 °C for 5 h. At last, the obtained products were washed with ethanol for several times and dried under vacuum at 60 °C for 8 h.

2.2.3. Synthesis of $\text{Au}/\text{Ni}_3\text{S}_2/\text{NF}$ catalysts

The final $\text{Au}/\text{Ni}_3\text{S}_2/\text{NF}$ sample was acquired by chemical reduction at room temperature. HAuCl_4 (100 μL) and $\text{Na}_3\text{C}_6\text{H}_5\text{O} \cdot 5\text{H}_2\text{O}$ (0.01 M) were dissolved into DIW (40 mL) and stirred evenly. Then, the $\text{Ni}_3\text{S}_2/\text{NF}$ and NaBH_4 (0.01 M) were put into it. After reaction for 1 h, the obtained $\text{Au}/\text{Ni}_3\text{S}_2/\text{NF}$ was washed by DIW and dried at 60 °C for 8 h under vacuum.

2.3. Material characterizations

X-ray diffraction (XRD) patterns were performed on X-ray diffractometer (Rigaku DMax- γ A) with Cu K α radiation ($\lambda = 1.5406 \text{ \AA}$). Scanning electron microscopic (SEM) images and energy dispersive spectrometry (EDS) were implemented through FEI Quanta-450 FEG. Transmission electron microscope (TEM) was conducted by a JEM-2010. The X-ray photoelectron spectroscopy (XPS) measurement was accomplished by ESCALAB 250Xi X-ray photoelectron spectrometer. The mole amount is obtained by Inductively coupled plasma-atomic emission spectroscopy (ICP-AES) data. The corresponding XANES and EXAFS data were gathered by Beamline 8-ID, National Synchrotron Light Source equipped with Si (111) monochromator and Lytle detector in Brookhaven National Laboratory.

2.4. Electrochemical measurements

Electrochemical measurements were achieved by CHI604E electrochemical analyzer with a typical three-electrode system comprising of the $\text{Au}/\text{Ni}_3\text{S}_2/\text{NF}$ sample as the working electrode, graphite rod electrode as the counter electrode and saturated calomel as the reference electrode. Meanwhile, two-electrode system using $\text{Au}/\text{Ni}_3\text{S}_2/\text{NF}$ sample as both the cathode and anode was utilized to estimate the performance of overall water splitting. All potentials mentioned in this work were revised to reversible hydrogen electrode (RHE) by means of Nernst equation. First, cyclic voltammograms (CVs) with different rate of 20 and 100 mV/s were applied to activate the working electrode. Then, the linear sweep voltammetry (LSV) curves were recorded at 5 mV/s with 95% iR-corrections to remove barrier of uncompensated resistance. Electrochemical impedance spectroscopy (EIS) measurement was conducted at the amplitude voltage of 5 mV by using ac impedance technology with range from 1 MHz to 10 mHz. To estimate double-layer capacitance (C_{dl}), CV measurement were achieved by different scan rates ranging from 25 to 150 mV in the potential windows -0.98 to -0.88 V for HER and 0 – 0.8 V for OER. Long-term stability tests were conducted using chronoamperometry under continuous potential. Additionally, 1.0 M KOH solution was used for above electrochemical test. The TOF value is obtained by following equation:

$$\text{TOF} = \frac{J \times A}{N \times F \times n} \quad (1)$$

where J is the measured current density, A is geometric area of the electrode, N is the number of electrons required for reaction, F is Faraday constant and n is the number of active sites. The electrochemical surface area (ECSA) of $\text{Au}/\text{Ni}_3\text{S}_2/\text{NF}$ and $\text{Ni}_3\text{S}_2/\text{NF}$ catalysts were estimated from their C_{dl} value. And the detailed ECSA is acquired by $\text{ECSA} = C_{\text{dl}}/C_s$, where C_s is the specific capacitance of the sample, which is usually between 20 and 60 $\mu\text{F cm}^{-2}$ and here we take the average value of 40 $\mu\text{F cm}^{-2}$ for calculation [34,35]. Subsequently, the normalized current density curve is obtained by the following formula:

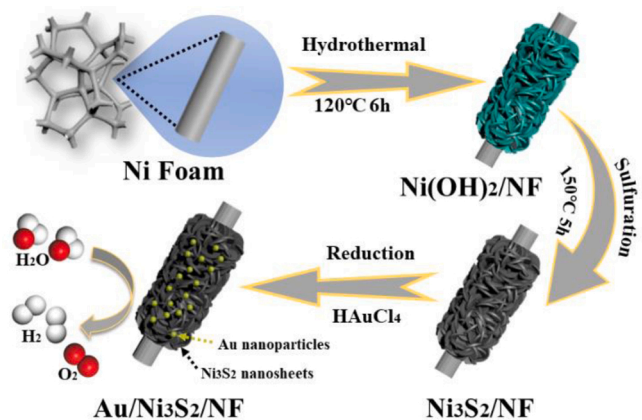


Fig. 1. Schematic illustration for the fabrication of Au/Ni₃S₂/NF.

$$j_{\text{ECSA}} = j/\text{ECSA}.$$

2.5. DFT calculation

All DFT calculations were accomplished by using Vienna Ab Initio Simulation Package (VASP), adopting the projector augmented wave (PAW) method [36]. The generalized gradient approximation (GGA) with Perdew-Burke-Ernzerhof (PBE) version was utilized to represent

the exchange and correlation energies [37]. A cut-off kinetic energy of 500 eV was selected for plane-wave basis functions and the $4 \times 4 \times 1$ Monkhorst-Pack grids were applied to all DFT optimizations [38]. The adjacent slabs were separated by a vacuum layer of 15 Å, which is sufficiently large to exclude the influence of models in vertical direction.

In overall HER pathway, the intermediate hydrogen would produced on the surface of electrocatalysts and the adsorption energy of intermediate hydrogen (ΔG_{H^*}) is the key indicator to evaluate HER catalytic activity and is achieved by following Eq. 1:

$$\Delta G_{\text{H}^*} = \Delta E_{\text{H}} + \Delta E_{\text{ZPE}} - T\Delta S_{\text{H}} \quad (2)$$

where ΔE_{H} , ΔE_{ZPE} and $T\Delta S_{\text{H}}$ are described the binding energy, zero-point energy change and entropy difference of hydrogen adsorption, respectively. Herein, the $\Delta E_{\text{ZPE}} - T\Delta S_{\text{H}}$ value is about 0.24 V reckoned by Norskov et al., which is represent the contribution of zero-point energy and entropy [39]. And ΔE_{H} is calculated by following Eq. (2):

$$\Delta E_{\text{H}} = E_{\text{surf+H}} - E_{\text{surf}} - 1/2E_{\text{H}_2} \quad (3)$$

where the $E_{\text{surf+H}}$ is the total energy of absorbed system, the E_{surf} and E_{H_2} are the energies of bare surface and gas phase species, respectively. Under alkaline condition, OER pathways include four fundamental steps as following:

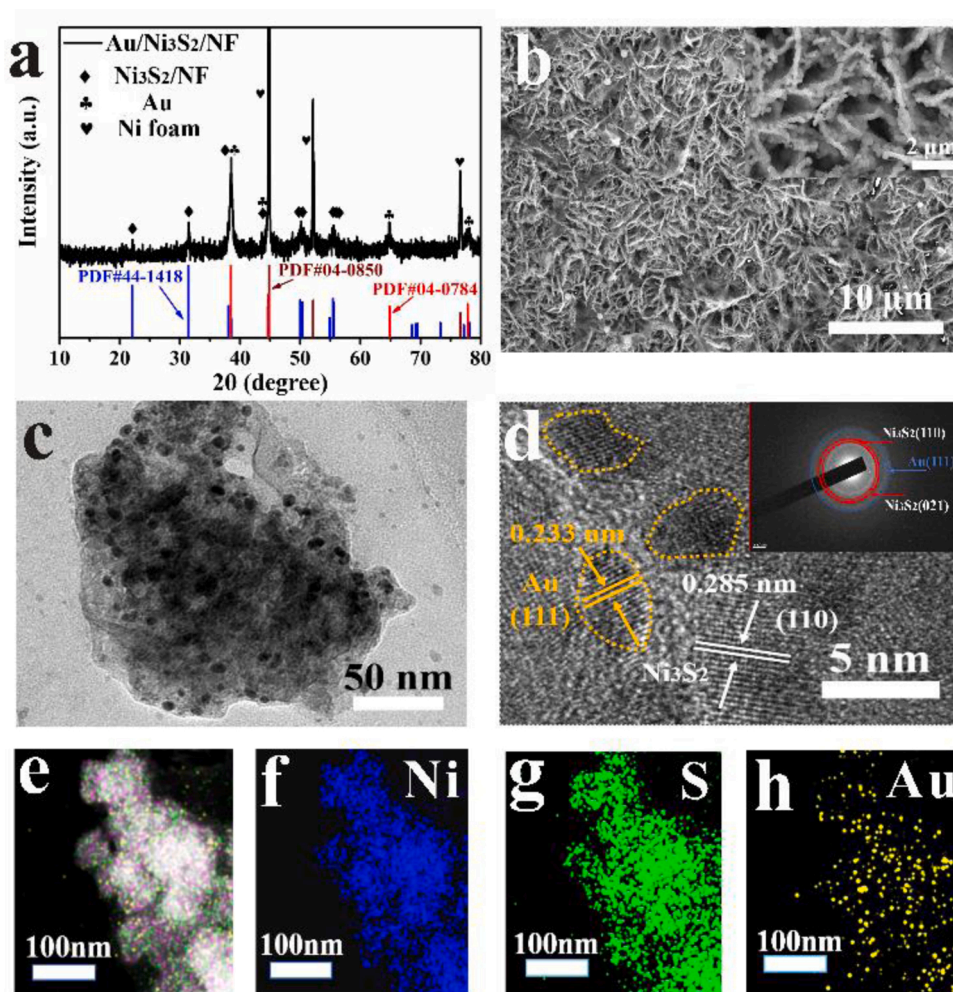


Fig. 2. (a) XRD pattern, (b) SEM image, (c)TEM image, (d) HRTEM image (inset is a SAED pattern), (e) STEM images of Au/Ni₃S₂/NF and its corresponding elemental mappings of (f) Ni (g) S and (h) Au.

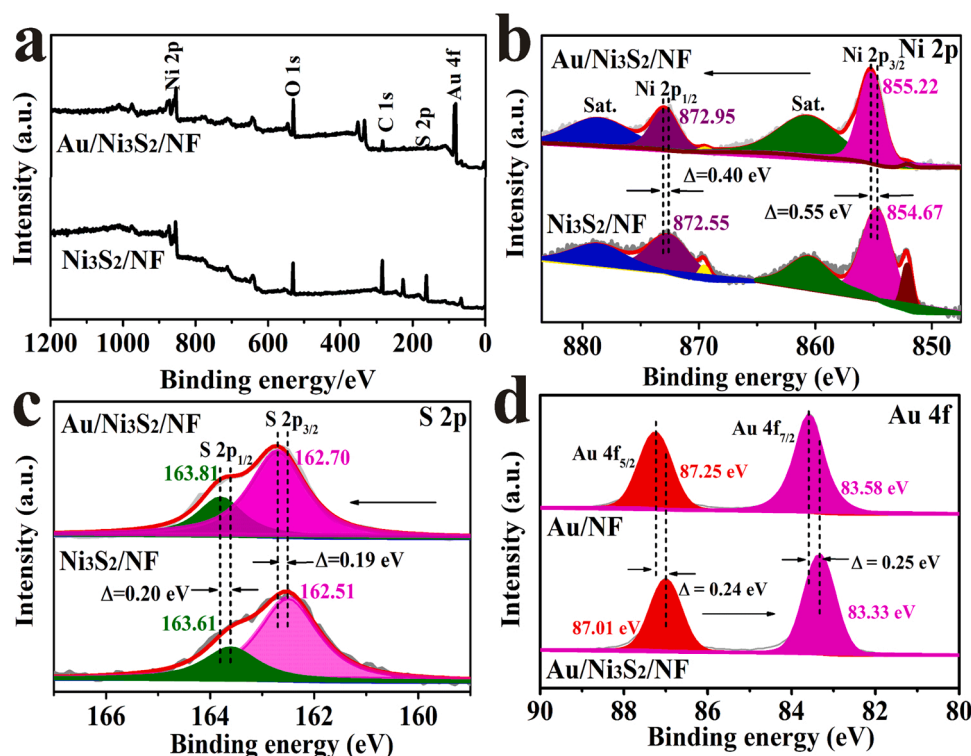


Fig. 3. (a) XPS spectra of Au/Ni₃S₂/NF and Ni₃S₂/NF (b) Ni 2p (c) S 2p XPS spectra of Au/Ni₃S₂/NF and Ni₃S₂/NF (d) Au 4f XPS spectra of Au/NF and Au/Ni₃S₂/NF.



As such, three intermediates consisting of OH*, O* and OOH* would produce on the surface of catalysts in OER process. And the Gibbs free energy of the adsorbed intermediates is also calculated by the similar equation ($\Delta G = \Delta E + \Delta E_{\text{ZPE}} - T\Delta S$).

3. Results and discussion

3.1. Morphology and microstructure analysis

The Au/Ni₃S₂/NF catalyst was fabricated through two-step hydrothermal process and then chemical reduction method, as illustrated in Fig. 1. Firstly, Ni(OH)₂/NF nanosheet arrays were directly synthesized on Ni foam substrates by hydrothermal method (Figs. S1 and S2), and then these nanosheet arrays were converted to Ni₃S₂/NF nanosheet arrays after hydrothermal sulfuration using 2-mercaptoethanol as precursor (Figs. S3 and S4). Finally, Au/Ni₃S₂/NF heterostructure electrocatalysts were obtained by chemical reduction of HAuCl₄ at room temperature. The exactly experimental process was illustrated in the experimental section.

To identify the crystal structure of the as-prepared Au/Ni₃S₂/NF sample, X-ray diffraction (XRD) characterization was employed. As presented in Fig. 2a, three dominant peaks appearing at 44.5°, 51.8° and 76.4° are assigned to pristine Ni foam substrate (JCPDS 04-0850) [40]. Additionally, other diffraction peaks are well matched with hexagonal heazlewoodite Ni₃S₂ (JCPDS 44-1418) and cubic Au (JCPDS 04-0784) [41–44]. Scanning electron microscopy (SEM) and transmission electron microscopy (TEM) were carried out to investigate the morphology

of Au/Ni₃S₂/NF. As displayed in Fig. 2b and its inset, the heterostructure catalyst is formed from perpendicularly interconnected nanosheets decorated with small nanoparticles. The TEM image (Fig. 2c) also validates that the typical heterostructure catalyst presents a nanosheet-like morphology, and some small nanoparticles with average size of 5.11 nm (Fig. S5) are uniformly anchored on the nanosheet, agreeing well with the SEM result. HRTEM image shown in Fig. 2d confirms that the nanosheet is Ni₃S₂ while the anchored nanoparticle is Au, since the clear lattice fringes with distance of 0.285 nm and 0.233 nm are corresponding to (110) facet of hexagonal Ni₃S₂ and (111) facet of cubic Au, respectively, which is consistent with the XRD results. The SAED pattern (inset in Fig. 2D) also verified the phase structure of heterostructure. Additionally, the STEM image (Fig. 2e) and its corresponding elemental mappings (Fig. 2f–h) prove that the heterostructure electrocatalyst involves Ni, S and Au elements, agreeing well with the EDS result in Fig. S6. The quantitative analysis results of catalysts in Table S1 show that the loading amount of Au in Au/Ni₃S₂/NF is about 4.69 wt%.

The chemical compositions and valence states of Au/Ni₃S₂/NF were revealed by X-ray photoelectron spectroscopy (XPS). As shown in Fig. 3a, the XPS survey spectra of Au/Ni₃S₂/NF testified the presence of elemental Ni, S, Au, which is also in accord with the EDS result (Fig. S6). As for the high-resolution Ni 2p spectra of Ni₃S₂/NF in Fig. 3b, two visible peaks located at the binding energy of 872.55 and 854.67 eV together with two satellite peaks are assigned to Ni 2p_{1/2} and Ni 2p_{3/2} orbitals of Ni²⁺ [45–47]. In addition, the other two peaks located at 852.8 and 869.8 eV are assigned to Ni⁰ from the Ni foam substrate, which has been demonstrated by the Ni 2p XPS spectra of the clean nickel foam (Fig. S7) [48,49]. Compared with Ni₃S₂/NF, the binding energies of Ni 2p_{1/2} and Ni 2p_{3/2} of Ni²⁺ in Au/Ni₃S₂/NF have a positive shift, implying a higher chemical valence of elemental Ni in the heterostructure, which also means a lower concentration of valence electron

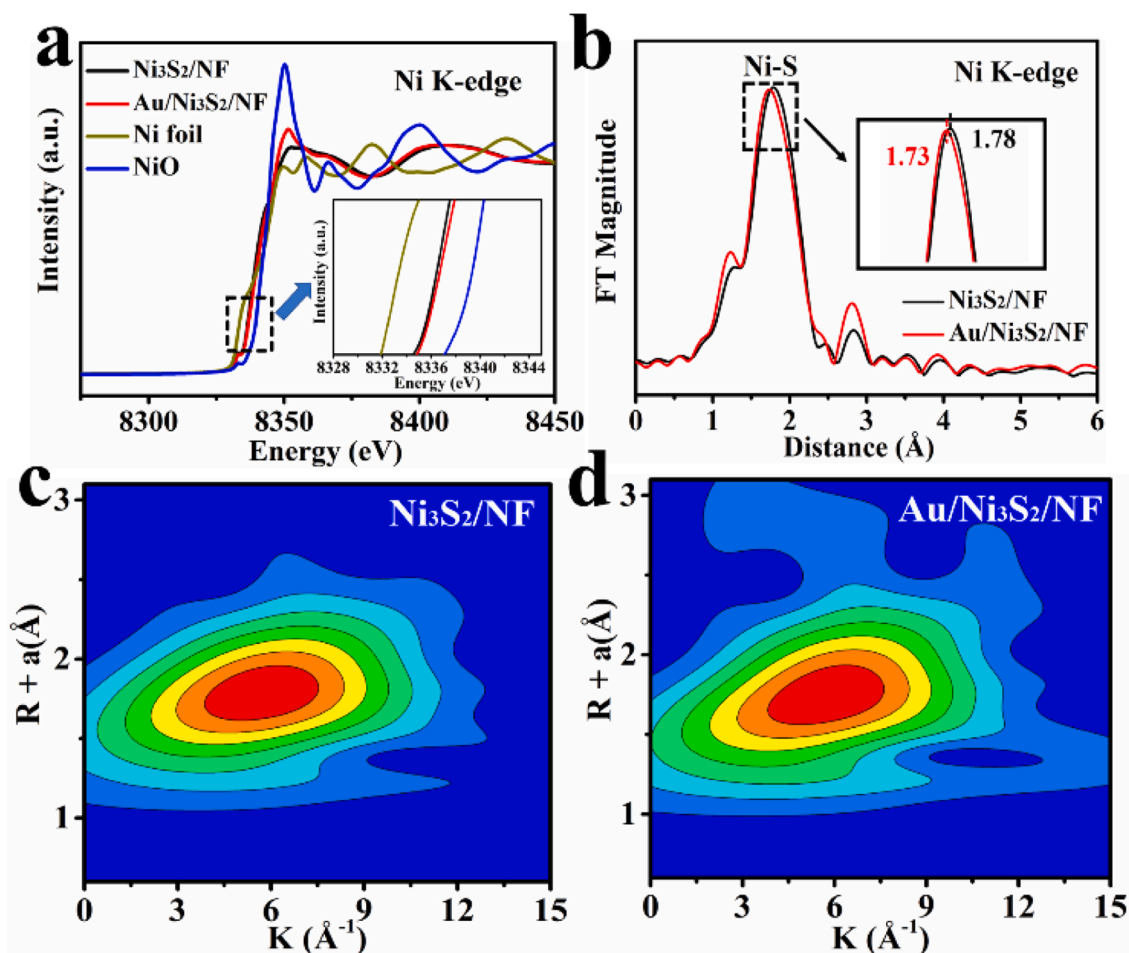


Fig. 4. (a) Ni K-edge XANES spectra of Ni₃S₂/NF and Au/Ni₃S₂/NF (b) FT curves in R space for Ni₃S₂/NF and Au/Ni₃S₂/NF (c–d) Wavelet transforms for Ni₃S₂/NF and Au/Ni₃S₂/NF, respectively.

around Ni atoms [50]. Moreover, the lower content of Ni⁰ species in Ni 2p spectra of Au/Ni₃S₂/NF compared with Ni₃S₂/NF may be attributed to the partial adsorption of X-ray energies by Au nanoparticles loaded on the surface of Ni₃S₂/NF, leading to that fewer signals of Ni⁰ species from NF substrate can be detected. Fig. 3c displays S 2p spectra of Au/Ni₃S₂/NF and Ni₃S₂/NF. Two prominent peaks of 163.81 and 162.70 eV assigned to S 2p_{1/2} and S 2p_{3/2} orbitals in Au/Ni₃S₂/NF have a positive shift in contrast to that in Ni₃S₂/NF, demonstrating a higher valence of elemental S in the heterostructure [51]. It can be observed that two peaks assigned to Au 4f_{5/2} and 4f_{7/2} of Au/Ni₃S₂/NF show a negative shift in comparison with Au/NF that is fabricated by the same chemical reduction process, suggesting a lower valence of Au in Au/Ni₃S₂/NF than that in Au/NF [52,53]. All these XPS results validate the charge transfer from Ni₃S₂ to Au at the interface of Au/Ni₃S₂/NF.

To further investigate the changes in the electron and coordination structure of Ni₃S₂ after hybridizing with Au nanoparticles, X-ray absorption near-edge structure (XANES) and extended X-ray absorption fine structure (EXAFS) were performed. The Ni K-edge XANES of Au/Ni₃S₂, along with Ni₃S₂, NiO and Ni foil as control samples, is depicted in Fig. 4a. Both the white line intensity and the absorption edge of Ni K-edge in Au/Ni₃S₂ is between Ni foil and NiO, suggesting the valence state of Ni in the heterostructure is in the valence state between 0 and + 2. Moreover, the white line intensity of Au/Ni₃S₂ is stronger than that of Ni₃S₂, indicating an increase in the Ni oxidation state in Au/Ni₃S₂ sample. And the inset of Fig. 4a exhibits that the absorption-edge of Ni in Au/Ni₃S₂ shifts positively in contrast to that in Ni₃S₂, also confirming a higher valence of Ni in Au/Ni₃S₂, which agrees well with the XPS analysis. Fig. 4b represents the Fourier transform k³-weighted EXAFS

spectra of Au/Ni₃S₂ and Ni₃S₂. The main peaks located at around 1.75 Å for both samples are corresponding to the nearest Ni—S bond [54]. The Ni—S bond length in Au/Ni₃S₂ (1.73 Å) is slightly smaller than that in Ni₃S₂ (1.78 Å), implying a stronger Ni—S bond strength, which is ascribed to the higher oxidation state of Ni in Au/Ni₃S₂ [55]. To quantitatively analysis the local coordination structure of Ni₃S₂ and Au/Ni₃S₂ including the coordination number and bond length of Ni atoms, the R space data have been fitted, which are shown in Fig. S8 and Table S2. It can be clearly observed that the coordination number of Au/Ni₃S₂ heterostructure (3.15) is almost unchanged relative to that of Ni₃S₂ (3.17), suggesting that Au is decorated on the surface of Ni₃S₂ rather than doping in its crystal lattice [56,57]. Moreover, the fitted R space data shown in Table S2 also manifests that the bond length of Au/Ni₃S₂ is shorter than the pristine Ni₃S₂. The Ni K-edge EXAFS wavelet transform (WT), which provides not only R space resolution but also k space resolution, was employed to investigate the atomic configuration of Ni₃S₂ and Au/Ni₃S₂ (Fig. 4c and d). The WT contour plots of Ni₃S₂ and Au/Ni₃S₂ display a maximum intensity at ~ 5.8 Å⁻¹ and ~ 6.1 Å⁻¹, both of which are assigned to Ni-S scattering [58].

3.2. Electrochemical catalytic performance

A typical three-electrode configuration was exploited to evaluate the HER and OER performance of Au/Ni₃S₂/NF electrodes in 1 M KOH solution. Figs. 5a and S9 shows the polarization curves of Au/Ni₃S₂/NF sample toward HER, along with NF, Ni₃S₂/NF and Pt/C as control samples. The overpotentials of Au/Ni₃S₂/NF at different current density (10, 20 and 100 mA cm⁻²) are 97, 120 and 196 mV, respectively, which

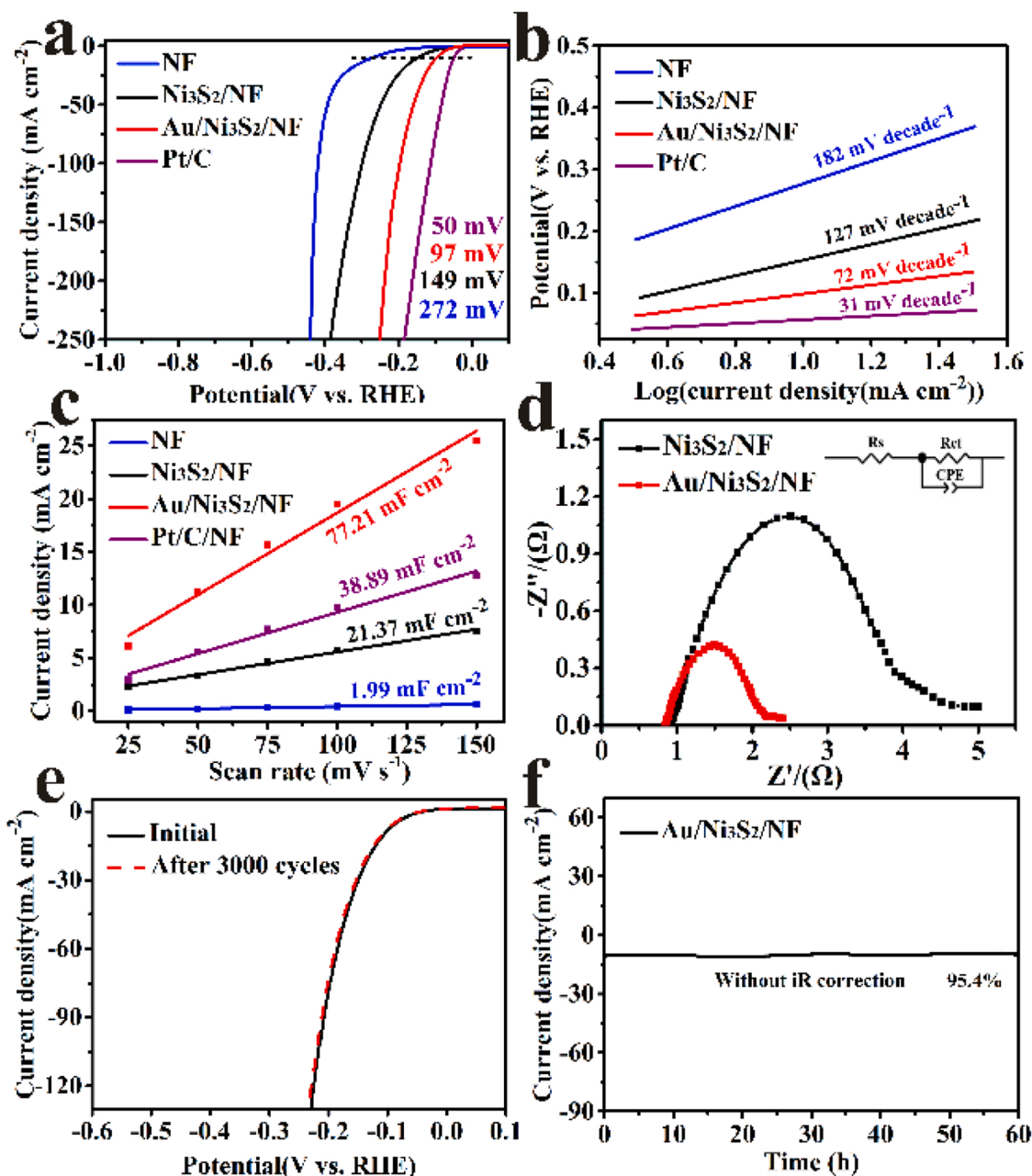


Fig. 5. (a) HER polarization curves (the dotted line represents the current density of -10 mA cm^{-2}), (b) Tafel plots, (c) Calculated electrochemical double-layer capacitances and (d) Nyquist plots (e) LSV curves of Au/Ni₃S₂/NF before and after 3000 CV cycles (f) Long-term stability test of Au/Ni₃S₂/NF under an overpotential of -130 mV for 60 h.

are obviously superior to that of Ni₃S₂/NF (149, 188 and 275 mV) and other reported nickel-based chalcogenides catalysts in Table S3 but is still inferior to commercial Pt/C. As is well known, Tafel slope is usually utilized to evaluate the reaction dynamics and HER pathway for HER [59,60]. As depicted in Fig. 5b, the Tafel slope of Au/Ni₃S₂/NF is 72 mV dec^{-1} , smaller than that of Ni₃S₂/NF (127 mV dec^{-1}), not only suggesting a faster kinetics but also implying a Volmer-Heyrovsky step [61]. The turnover frequency (TOF) is an effective index to measure the intrinsic per-site activity of the catalyst [62]. As shown in Fig. S10, the TOF value of Au/Ni₃S₂ is evidently larger than that of Ni₃S₂, indicating that the decorated Au can enhance the intrinsically catalytic activity of Ni₃S₂. In order to evaluate the electrochemically active surface areas (ECSA) of Au/Ni₃S₂/NF, the double-layer capacitances (C_{dl}) measured by cyclic voltammetry (CV) with different scan rate were estimated, because of the linear relation between ECSA and C_{dl} , as illustrated in

Fig. 5c. It can be observed that Au/Ni₃S₂/NF electrode possesses a larger C_{dl} (77.21 mF cm^{-2}) than Ni₃S₂/NF (21.37 mF cm^{-2}), Ni foam (1.99 mF cm^{-2}) and Pt/C/NF (38.89 mF cm^{-2}), demonstrating more active sites, which is favorable for HER. To exclude the contribution of ECSA for the HER activity and identify the intrinsic activity of the heterostructure, the ECSA-normalized activity of Au/Ni₃S₂/NF and Ni₃S₂/NF was presented in Fig. S11, which also validated that Au/Ni₃S₂/NF possessed better intrinsic activity than Ni₃S₂/NF. To further reveal the electrode kinetics, electrochemical impedance spectroscopy (EIS) test was performed. Fig. 5d shows the Nyquist plots of Au/Ni₃S₂/NF and Ni₃S₂/NF, as well as an equivalent circuit. It can be observed that the R_{ct} value of Au/Ni₃S₂/NF (1.13Ω) is smaller than that of Ni₃S₂/NF (4.08Ω), implying a faster charge transfer at the interface of electrode and electrolyte during HER [63]. Besides catalytic activity, the good stability is another evaluation parameter for an ideal catalyst

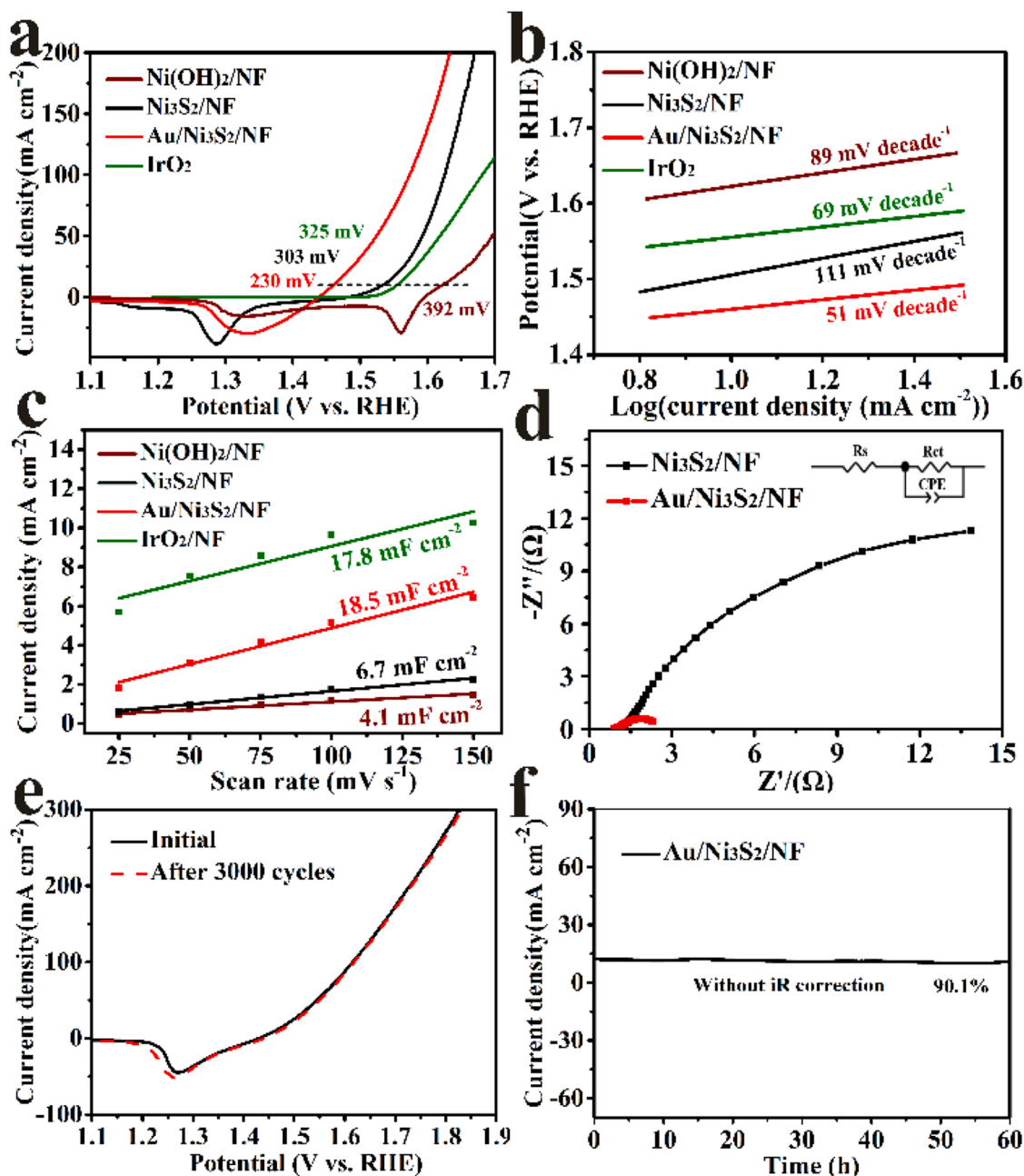


Fig. 6. (a) OER polarization curves (the dotted line represents the current density of 10 mA cm^{-2}), (b) Tafel plots, (c) Calculated electrochemical double-layer capacitances, (d) Nyquist plots of Ni_3S_2 and $\text{Au/Ni}_3\text{S}_2$ toward OER, (e) LSV curves of $\text{Au/Ni}_3\text{S}_2/\text{NF}$ before and after 3000 CV cycles and (f) Long-term stability test of $\text{Au/Ni}_3\text{S}_2/\text{NF}$ under the constant overpotential of 250 mV for 60 h.

[64,65]. As displayed in Fig. 5e, the LSV curve of $\text{Au/Ni}_3\text{S}_2/\text{NF}$ shows negligible change after 3000 CV cycles, suggesting its excellent stability. We also performed long-term durability test by means of chronoamperometry measurement with an applied overpotential of -130 mV up to a long period of 60 h (Fig. 5f), and the final current density could sustain 95.4%. Moreover, the chronoamperometry measurement at a higher current density around 200 mA cm^{-2} for 120 h was also carried out (Fig. S12). After test, the current density of the heterostructure electrode can maintain 87.3%, which is superior to most of Ni-based compound catalysts towards HER [66].

The OER performance of $\text{Au/Ni}_3\text{S}_2/\text{NF}$ is also measured in 1 M KOH, as well as $\text{Ni}_3\text{S}_2/\text{NF}$, $\text{Ni(OH)}_2/\text{NF}$ and commercial IrO_2 decorated on NF with the same mass loading. As revealed in Figs. 6a and S13, $\text{Au/Ni}_3\text{S}_2/\text{NF}$ exhibits impressively enhanced OER activity, only requiring low

overpotentials of 230, 258 and 386 mV at 10, 20 and 100 mA cm^{-2} , respectively, which is better than $\text{Ni}_3\text{S}_2/\text{NF}$ (303, 328 and 396 mV), $\text{Ni(OH)}_2/\text{NF}$ (392, 418 and 500 mV) and IrO_2/NF (325, 346 and 450 mV). Additionally, $\text{Au/Ni}_3\text{S}_2/\text{NF}$ also possesses the smallest Tafel slope (51 mV dec^{-1}) among all the samples (Fig. 6b), also implying the fastest kinetics. In a word, the obtained $\text{Au/Ni}_3\text{S}_2/\text{NF}$ heterostructure catalyst presents distinguished alkaline OER activity, which is superior to most of nickel-based chalcogenides catalysts recently reported, as shown in Table S4. Furthermore, as observed in Fig. 6c, C_{dl} of $\text{Au/Ni}_3\text{S}_2/\text{NF}$ (18.5 mF cm^{-2}) is higher than $\text{Ni}_3\text{S}_2/\text{NF}$ (6.7 mF cm^{-2}), $\text{Ni(OH)}_2/\text{NF}$ (4.1 mF cm^{-2}) and IrO_2/NF (17.8 mF cm^{-2}), demonstrating more ECSA for OER process. To clarify the intrinsic activity of $\text{Au/Ni}_3\text{S}_2/\text{NF}$, the specific activity (ECSA-normalized) of $\text{Au/Ni}_3\text{S}_2/\text{NF}$ is shown in Fig. S14, also demonstrating its better intrinsic OER activity than $\text{Ni}_3\text{S}_2/\text{NF}$.

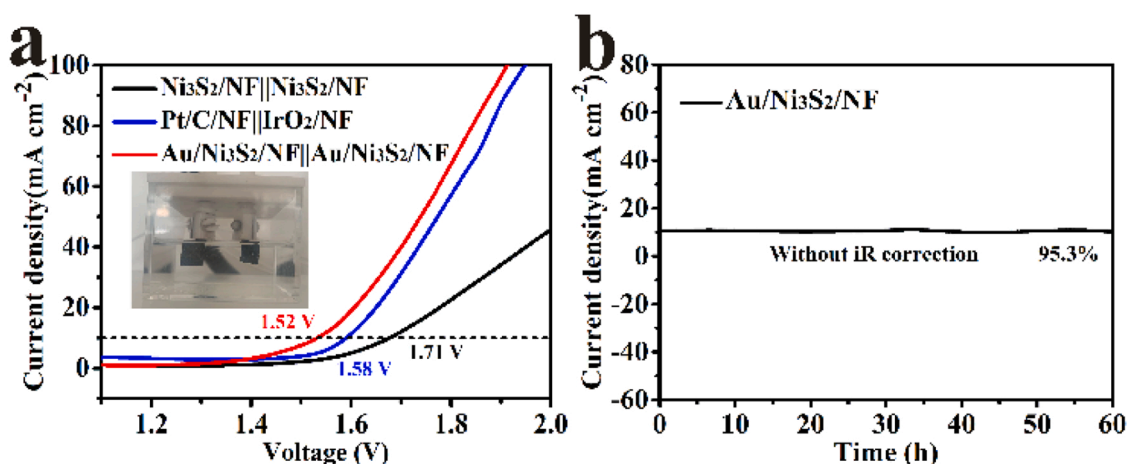


Fig. 7. (a) Schematic illustration of two-electrode cell using $\text{Au}/\text{Ni}_3\text{S}_2/\text{NF}$ for both anode and cathode for water splitting. (b) Long-term stability test of $\text{Au}/\text{Ni}_3\text{S}_2/\text{NF}$ under the constant overpotential of 450 mV for 60 h.

NF. Observed from the EIS result (Fig. 6d), $\text{Au}/\text{Ni}_3\text{S}_2/\text{NF}$ possesses obviously lower charge-transfer resistance (1.39Ω) comparing with $\text{Ni}_3\text{S}_2/\text{NF}$ (12.20Ω), suggesting a more rapid charge transfer between the electrode and electrolyte. To evaluate the stability of the catalysts during OER, the LSV curve of $\text{Au}/\text{Ni}_3\text{S}_2/\text{NF}$ after 3000 CV cycles is tested (Fig. 6e), which has scarcely any changes in contrast to that of $\text{Ni}_3\text{S}_2/\text{NF}$, indicating its excellent stability. In addition, the durability test of $\text{Au}/\text{Ni}_3\text{S}_2/\text{NF}$ shows that the current density under the overpotential of 350 mV after 60 h operation can sustain 90.1% (Fig. 6f). And the long-term stability of $\text{Au}/\text{Ni}_3\text{S}_2/\text{NF}$ towards OER under a high current density of $\sim 200 \text{ mA}$ was also performed (Fig. S15). The current density of the electrode can maintain 85.6% after 120 h test, suggesting an unexceptionable durability even at a high current density. Recent studies revealed that most of nickel-based non-oxides catalysts couldn't endure high redox potential during OER and would partially or completely transform into nickel (oxy)hydroxides [67–69]. The $\text{Au}/\text{Ni}_3\text{S}_2/\text{NF}$ electrocatalyst after long-term OER test was further characterized by SEM, TEM, XPS and XRD. As shown in Fig. S16, SEM results demonstrated that the $\text{Au}/\text{Ni}_3\text{S}_2/\text{NF}$ catalyst still maintained its initial nanosheet structure. The TEM and HRTEM image suggested that an amorphous layer formed on the surface of post-treated catalyst, confirming the existence of the superficial oxidation, which is consistent with other works reported recently [70,71]. XPS investigation (Fig. S17) was applied to reveal the elemental composition and existed form of the superficial layer after long-term OER test. The Ni 2p spectrum verifies the superficial oxidation, of which two peaks concentrated at 856.3 and 874.9 eV are assigned to nickel (oxy)hydroxide [72]. And the S 2p XPS spectra of the heterostructure after OER test shows that elemental S is remained in the surface of the post-treated heterostructure, which exists in the form of sulfate and Ni_3S_2 , since the binding energies of S 2p orbit (168.5 , 163.8 and 162.4 eV) are assigned to sulfate and Ni_3S_2 , respectively (Fig. S17c) [70]. Significantly, XRD pattern after OER test (Fig. S17e) shows no new diffraction peaks, also confirming the amorphous oxide formed on the surface of $\text{Au}/\text{Ni}_3\text{S}_2/\text{NF}$.

In consideration of the outstanding HER and OER catalytic activity and stability of $\text{Au}/\text{Ni}_3\text{S}_2/\text{NF}$, we rationally speculated that the bifunctional electrocatalyst could be utilized to split water efficiently. Therefore, a two-electrode water splitting configuration using $\text{Au}/\text{Ni}_3\text{S}_2/\text{NF}$ as both the cathode and anode was constructed in 1.0 M KOH . As shown in Fig. 7a, this electrolytic tank only needs a low cell voltage of 1.52 V to achieve the current density of 10 mA cm^{-2} , which is better than that using $\text{Ni}_3\text{S}_2/\text{NF}$ as electrodes ($1.71 \text{ V}@10 \text{ mA cm}^{-2}$), and is even superior to $\text{Pt}/\text{C}||\text{IrO}_2$ counterpart ($1.58 \text{ V}@10 \text{ mA cm}^{-2}$) and most of bifunctional electrocatalysts recently reported in Table S5. Furthermore, the long-term durability was estimated by the constant overpotential of

450 mV and the chronoamperometry curve in Fig. 7b showed negligible degradation up to 60 h test. Even tested at a high current density of $\sim 200 \text{ mA cm}^{-2}$, the electrolytic cell also exhibits an excellent stability, which can sustain 89.6% after 120 h test, as shown in Fig. S18. On account of its excellent bifunctional catalytic performance towards water splitting, $\text{Au}/\text{Ni}_3\text{S}_2/\text{NF}$ may be a promising alternative for future alkaline water splitting.

3.3. Theoretical calculations

To deeply uncover the synergistic effect of $\text{Au}/\text{Ni}_3\text{S}_2$ heterostructure interface, we carried out density functional theory (DFT) calculations. To sensibly construct $\text{Au}-\text{Ni}_3\text{S}_2$ heterostructure catalyst by strain analysis, Au (111) plane and Ni_3S_2 (001) plane were selected as the heterostructure interface based on its small lattice strain ($\sim 0.47\%$) [30,73,74]. The schematic models of Ni_3S_2 and $\text{Au}/\text{Ni}_3\text{S}_2$ heterostructure catalyst were shown in Fig. S19, respectively. In order to distinctly identify the electronic interaction at the interface of the heterostructure, the differential charge density of $\text{Au}/\text{Ni}_3\text{S}_2$ interface was presented in Fig. 8a. It can be expressly seen that the electrons at the interface are gathered on the side of Au, which may be attributed to a higher work function of Au than Ni_3S_2 . Similarly, the quantitative Bader charge analysis illustrated in Fig. S20 demonstrate that the electronic number around Au site is increased from 11.004 e to 11.092 e , while the electronic number around Ni/S site are decreased from $9.653/6.523 \text{ e}$ to $9.621/6.434 \text{ e}$, respectively, agreeing well with the XPS and XAFS analysis. Fig. 8b showed the total densities of states (DOS) of $\text{Au}/\text{Ni}_3\text{S}_2$ and pristine Ni_3S_2 . It can be seen that both of samples have a continuous DOS around the Fermi level, indicating their metallic property [75]. Moreover, $\text{Au}/\text{Ni}_3\text{S}_2$ that possesses a higher DOS around the Fermi level has a better electrical conductivity than Ni_3S_2 , which is beneficial for both HER and OER [76,77]. In terms of HER in alkaline media, the adsorption and dissociation of H_2O on active sites is crucial, especially for Ni_3S_2 , which is considered as a bottleneck [78]. As illustrated in Fig. 8c, the energy barrier of $\text{Au}/\text{Ni}_3\text{S}_2$ toward water dissociation is 3.268 eV , which is lower than that of Ni_3S_2 (3.498 eV). In addition, the free energy of intermediate H^* adsorption (ΔG_{H^*}) for different sites of Ni_3S_2 and $\text{Au}/\text{Ni}_3\text{S}_2$ were calculated in Fig. 8d. The ΔG_{H^*} value on Ni/S site of $\text{Au}/\text{Ni}_3\text{S}_2$ is 0.35 and 0.03 eV , which are both lower than Ni/S site of Ni_3S_2 (0.4 and 1.30 eV), indicating $\text{Au}/\text{Ni}_3\text{S}_2$ heterostructure can strength the binding with H intermediate and enhance the intrinsic activity. Similarly, DFT calculations were also conducted to account for the enhancement of the intrinsic OER activity of $\text{Au}/\text{Ni}_3\text{S}_2$. The diagrammatic structure models of intermediates ($^*\text{OH}$, $^*\text{O}$, and $^*\text{OOH}$) adsorbed on Ni site was illustrated in Fig. S14b. The OER pathway of Ni_3S_2 and

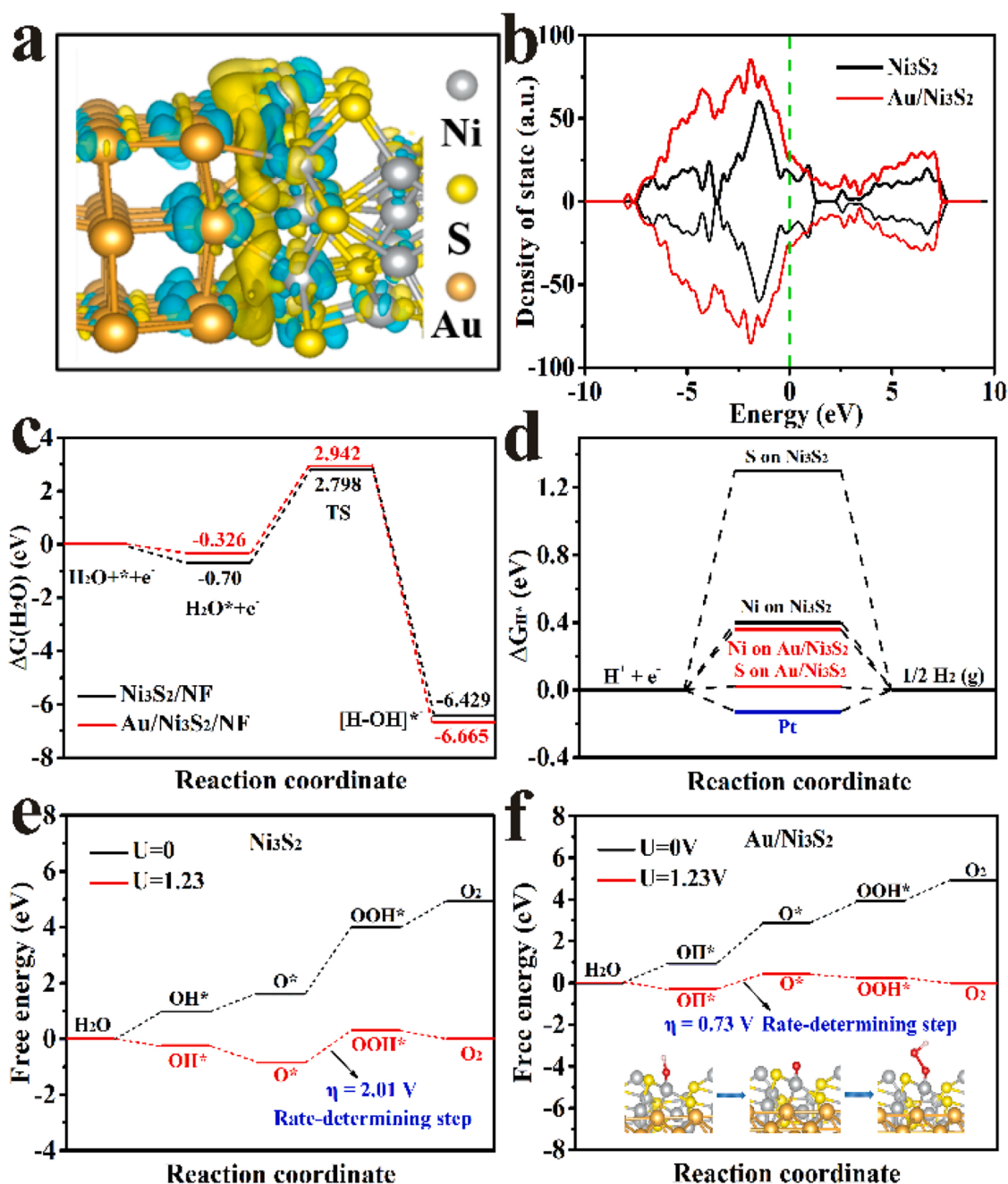


Fig. 8. (a) Charge density difference profile at the Au/Ni₃S₂ interface; Yellow and blue region represent electron accumulation and loss. (b) the Total DOS of Au/Ni₃S₂ and Ni₃S₂ sample. (c) Calculated adsorption free energy diagrams for the Volmer step of Ni₃S₂ and Au/Ni₃S₂ (d) Free energy diagram of Au/Ni₃S₂ and Ni₃S₂ on different sites for HER. (e–f) Calculated free energy pathway of Ni₃S₂ and Au/Ni₃S₂ toward OER.

Au/Ni₃S₂ were displayed in Fig. 8e and f, respectively, which summarized the Gibbs free energy of different oxygen-contained intermediates including OH^* , O^* , and OOH^* . Fig. 8e indicated that the rate-determining step of Ni₃S₂ is the transformation process from O^* to OOH^* , with an overpotential as high as 1.15 V, hindering the evolution of oxygen. After hybridizing with Au, the rate-determining step of the heterostructure had become from OH^* to O^* , and the overpotential is remarkably decreased to 0.73 V, suggesting an accelerated OER kinetics. Consequently, the strong electronic coupling at the interface of the heterostructure of Au/Ni₃S₂ can modulate the electronic structure that not only increases its conductivity, but also optimizes the adsorption free energies of intermediates for both HER and OER, resulting in the enhanced intrinsic HER/OER activity.

4. Conclusions

In summary, we rationally constructed a heterostructure catalyst of Au/Ni₃S₂/NF nanosheet arrays that exhibits an outstanding bifunctional activity and stability towards HER and OER. Combining the advanced X-ray spectrum analysis including XPS and XAFS with DFT calculations, it was revealed that the electronic interaction at the interface of the heterostructure could optimize the electronic structure, which could increase the conductivity, reduce the dissociation energy of H_2O , as well as optimize the adsorption free energy of H/O intermediates during HER and OER process, respectively, finally resulting in the obviously boosted HER and OER performance. Inspiringly, an alkaline electrolyte tank utilizing Au/Ni₃S₂/NF as both cathode and anode exhibited excellent activity that only required a cell voltage of 1.52 V to drive a current

density of 10 mA cm⁻² in 1 M KOH, and sustained a long-term durability up to 60 h. This work rationally constructs heterostructure interfaces, which provides insights into fabricating advanced bifunctional electrocatalysts for overall water splitting including transition-metal sulfides, selenides, phosphides and beyond.

CRediT authorship contribution statement

H. Liu supervised this work, revised the manuscript and was responsible for formal analysis. J. Cheng carried out the experiments, wrote the original manuscript and data analysis. W. He and Y. Li conducted DFT calculations and assisted the data analysis. X. Zheng, C. Chen, C. Cui, and Q. Hao provided resources and assisted the data discussion. All authors contributed to the discussion and declared no conflict of interest.

Declaration of Competing Interest

The authors declare that they have no known competing financial interests or personal relationships that could have appeared to influence the work reported in this paper.

Acknowledgments

The authors gratefully acknowledge the financial support from Natural Science Foundation of Hebei Province (E2019202206, E2020202114, B2021202019) and National Natural Science Foundation of China (51402085).

Appendix A. Supplementary material

Supplementary data associated with this article can be found in the online version at doi:10.1016/j.apcatb.2021.120935.

References

- [1] Z.W. Seh, J. Kibsgaard, C.F. Dickens, I. Chorkendorff, J.K. Nørskov, T.F. Jaramillo, *Science* 355 (2017) 146.
- [2] Y. Wang, X. Li, M. Zhang, Y. Zhou, D. Rao, C. Zhong, J. Zhang, X. Han, W. Hu, Y. Zhang, K. Zaghib, Y. Wang, Y. Deng, *Adv. Mater.* 32 (2020), 2000231.
- [3] Z. Wang, W. Xu, X. Chen, Y. Peng, Y. Song, C. Lv, H. Liu, J. Sun, D. Yuan, X. Li, X. Guo, D. Yang, L. Zhang, *Adv. Funct. Mater.* 29 (2019), 1902875.
- [4] X. Zhang, S. Zhang, J. Li, E. Wang, *J. Mater. Chem. A* 5 (2017) 22131–22136.
- [5] L. Wu, L. Yu, F. Zhang, B. Mcelhenny, D. Luo, A. Karim, S. Chen, Z. Ren, *Adv. Funct. Mater.* 31 (2020), 2006484.
- [6] H. Zhang, W. Maijenburg, X. Li, S.L. Schweizer, R.B. Wehrspohn, *Adv. Funct. Mater.* 30 (2020), 2003261.
- [7] L. Ji, J. Wang, X. Teng, T.J. Meyer, Z. Chen, *ACS Catal.* 10 (2020) 412–419.
- [8] M. Gong, W. Zhou, M.C. Tsai, J. Zhou, M. Guan, M.C. Lin, B. Zhang, Y. Hu, D. Y. Wang, *J. Yang, Nat. Commun.* 5 (2014) 4695.
- [9] L. Wen, X. Shan, J. Liu, H. Mu, L. Jiang, *Angew. Chem. Int. Ed.* 59 (2020), 1659–1655.
- [10] C. Zhao, Z. Chen, R. Shi, X. Yang, T. Zhang, *Adv. Mater.* 32 (2020), 1907296.
- [11] W. Liu, E. Hu, H. Jiang, Y. Xiang, Z. Weng, M. Li, Q. Fan, X. Yu, E.I. Altman, H. Wang, *Nat. Commun.* 7 (2016) 10771.
- [12] H. Guo, Z. Fang, H. Li, D. Fernandez, G. Henkelman, S.M. Humphrey, G. Yu, *ACS Nano* 13 (2019) 13225–13234.
- [13] M. Li, Y. Zhu, H. Wang, C. Wang, N. Pinna, X. Lu, *Adv. Energy Mater.* 9 (2019), 1803185.
- [14] J. Yin, J. Jin, H. Zhang, M. Lu, Y. Peng, B. Huang, P. Xi, C.H. Yan, *Angew. Chem. Int. Ed.* 131 (2019) 18676–18682.
- [15] H. Zhang, J. Wang, Q. Cheng, P. Saha, H. Jiang, *Green Energy Environ.* 5 (2020) 492–498.
- [16] Z.P. Wu, X.F. Lu, S.Q. Zang, X.W. Lou, *Adv. Funct. Mater.* 30 (2020), 1910274.
- [17] T. Zhao, X. Shen, Y. Wang, R.K. Hocking, Y. Li, C. Rong, K. Dastafkan, Z. Su, C. Zhao, *Adv. Funct. Mater.* 31 (2021), 2100614.
- [18] H. Jin, Q. Gu, B. Chen, C. Tang, Y. Zheng, H. Zhang, M. Jaroniec, S.Z. Qiao, *Chem* 6 (2020) 2382–2394.
- [19] W. Zhou, X.J. Wu, X. Cao, X. Huang, C. Tan, J. Tian, H. Liu, J. Wang, H. Zhang, *Energy Environ. Sci.* 6 (2013) 2921–2924.
- [20] L.L. Feng, G. Yu, Y. Wu, G.D. Li, H. Li, Y. Sun, T. Asefa, W. Chen, X. Zou, *J. Am. Chem. Soc.* 137 (2015) 14023–14026.
- [21] J. Zhang, T. Wang, D. Pohl, B. Rellinghaus, R. Dong, S. Liu, X. Zhuang, X. Feng, *Angew. Chem. Int. Ed.* 55 (2016) 6702–6707.
- [22] T. Kou, T. Smart, B. Yao, I. Chen, D. Thota, Y. Ping, Y. Li, *Adv. Energy Mater.* 8 (2018), 1703538.
- [23] J.X. Feng, J.Q. Wu, Y.X. Tong, G.R. Li, *J. Am. Chem. Soc.* 140 (2017) 610–617.
- [24] W. He, L. Han, Q. Hao, X. Zheng, Y. Li, J. Zhang, C. Liu, H. Liu, H.L. Xin, *ACS Energy Lett.* 4 (2019) 2905–2912.
- [25] D. Jia, L. Han, Y. Li, W. He, C. Liu, J. Zhang, C. Chen, H. Liu, H.L. Xin, *J. Mater. Chem. A* 8 (2020) 18207–18214.
- [26] Y. Xiong, L. Xu, C. Jin, Q. Sun, *Appl. Catal. B-Environ.* 254 (2019) 329–338.
- [27] Y. Zhang, J. Fu, H. Zhao, R. Jiang, R. Jiang, F. Tian, R. Zhang, *Appl. Catal. B-Environ.* 257 (2019), 117899.
- [28] M. Lee, H.S. Oh, M.K. Cho, J.P. Ahn, Y.J. Hwang, B.K. Min, *Appl. Catal. B-Environ.* 233 (2018) 130–135.
- [29] L. Han, S. Dong, E. Wang, *Adv. Mater.* 28 (2016) 9266–9291.
- [30] C. Liu, F. Wang, D. Jia, J. Zhang, J. Zhang, Q. Hao, J. Zhang, Y. Li, H. Liu, *Nanoscale* 12 (2020) 19333–19339.
- [31] P. Wang, X. Zhang, J. Zhang, S. Wan, S. Guo, G. Lu, J. Yao, X. Huang, *Nat. Commun.* 8 (2017) 14580.
- [32] S. Zhao, R. Jin, H. Abroshan, C. Zeng, H. Zhang, S.D. House, E. Gottlieb, H.J. Kim, J.C. Yang, R. Jin, *J. Am. Chem. Soc.* 139 (2017) 1077–1080.
- [33] Z. Pan, M. Liu, P. Niu, F. Guo, X. Fu, X. Wang, *Acta Phys.-Chim. Sin.* 36 (2020), 1906014.
- [34] M.A. Lukowski, A.S. Daniel, C.R. English, M. Fei, A. Forticaux, R.J. Harriers, J. Song, *Energy Environ. Sci.* 7 (2014) 2608–2613.
- [35] H. Liang, A.N. Gandi, D.H. Anjum, X. Wang, U. Schwingenschlogl, H.N. Alshareef, *Nano Lett.* 16 (2016) 7718–7725.
- [36] G. Kresse, J. Furthmüller, *Phys. Rev. B* 54 (1996) 11169.
- [37] K. Qi, X. Cui, L. Gu, S. Yu, X. Fan, M. Luo, S. Xu, N. Li, L. Zheng, Q. Zhang, J. Ma, Y. Gong, F. Lv, K. Wang, H. Huang, W. Zhang, S. Guo, W. Zheng, P. Liu, *Nat. Commun.* 10 (2019) 5231.
- [38] H.J. Monkhorst, J.D. Pack, *Phys. Rev. B* 13 (1976) 5188.
- [39] J.K. Noerskov, T. Bligaard, A. Logadottir, J.R. Kitchin, J.G. Chen, S. Pandalov, U. Stimming, *Cheminform* 36 (2005), e12154.
- [40] G. Ren, Q. Hao, J. Mao, L. Liang, H. L. C. Liu, *Nanoscale* 10 (2018) 17347–17353.
- [41] H. Du, R. Kong, F. Qu, L. Lu, *Chem. Commun.* 54 (2018) 10100–10103.
- [42] N. Cheng, Q. Liu, A.M. Asiri, W. Xing, X. Sun, *J. Mater. Chem. A* 3 (2015) 23207–23212.
- [43] H. Liao, Y. Sun, C. Dai, Y. Du, S. Xi, F. Liu, L. Yu, Z. Yang, Y. Hou, A.C. Fisher, S. Li, Z.J. Xu, *Nano Energy* 50 (2018) 273–280.
- [44] H. Lv, X. Zheng, Z. Chen, S. Guo, Y. Yu, W. Zhu, Q. Li, X. Zhang, M. Pan, G. Lu, S. Mu, S. Sun, *J. Am. Chem. Soc.* 137 (2015) 5859–5862.
- [45] B. Fei, Z. Chen, J. Liu, H. Xu, X. Yan, H. Qing, M. Chen, R. Wu, *Adv. Energy Mater.* 10 (2020), 2001963.
- [46] P. Ganesan, A. Sivanantham, S. Shanmugam, *J. Mater. Chem. A* 4 (2016) 16394–16402.
- [47] P. Zhai, Y. Zhang, Y. Wu, J. Gao, B. Zhang, S. Cao, Y. Zhang, Z. Li, L. Sun, J. Hou, *Nat. Commun.* 11 (2020) 5462.
- [48] N. Chen, Y. Du, G. Zhang, W. Lu, F. Cao, *Nano Energy* 81 (2021), 105605.
- [49] J. Wang, P. He, Y. Shen, L. Dai, Z. Li, Y. Wu, C. An, *Nano Res.* 14 (2021) 3474–3481.
- [50] Y. Wu, X. Liu, D. Han, X. Song, L. Shi, Y. Song, S. Niu, Y. Xie, J. Cai, S. Wu, J. Kang, J. Zhou, Z. Chen, X. Zheng, X. Xiao, G. Wang, *Nat. Commun.* 9 (2018) 1425.
- [51] B. Dong, X. Zhao, G.Q. Han, X. Li, X. Shang, Y.R. Liu, W.H. Hu, Y.M. Chai, H. Zhao, C.G. Liu, *J. Mater. Chem. A* 4 (2016) 13499–13508.
- [52] Shi Yi, J. Wang, C. Wang, T.T. Zhai, W.J. Bao, J.J. Xu, X. Xia, H.Y. Chen, *J. Am. Chem. Soc.* 137 (2015) 7365–7370.
- [53] S. Zhao, R. Jin, Y. Song, H. Zhang, S.D. House, J.C. Yang, R. Jin, *Small* 13 (2017), 1701519.
- [54] H. Zhang, L. Yu, W. Zhou, X.W. Lou, *Adv. Funct. Mater.* 28 (2018), 1807086.
- [55] S.D. Kelly, N. Yang, G.E. Mickelson, N. Greenlay, E. Karapetrova, W. Sinkler, S. R. Bare, *J. Catal.* 263 (2009) 16–33.
- [56] T. Ling, T. Zhang, B. Ge, L. Han, L. Zheng, F. Lin, Z. Xu, W.B. Hu, X.W. Du, K. Davey, S.Z. Qiao, *Adv. Mater.* 31 (2019), 1807771.
- [57] F. Gong, S. Ye, M. Liu, J. Zhang, L. Gong, G. Zeng, E. Meng, P. Su, K. Xie, Y. Zhang, J. Liu, *Nano Energy* 78 (2020), 105284.
- [58] D.W. Su, J. Ran, Z.W. Zhuang, C. Chen, S.Z. Qiao, Y.D. Li, G.X. Wang, *Sci. Adv.* 6 (2020) eaaz8447.
- [59] D. Kong, J.J. Cha, H. Wang, H.R. Lee, Y. Cui, *Energy Environ. Sci.* 6 (2013) 3553–3558.
- [60] C. Ouyang, X. Wang, C. Wang, X. Zhang, J. Wu, Z. Ma, S. Dou, S. Wang, *Electrochim. Acta* 174 (2015) 297–301.
- [61] K. Lu, Y. Liu, F. Lin, I.A. Cordova, S. Gao, B. Li, B. Peng, J. Kaelin, D. Coliz, C. Wang, Y. Shao, Y. Cheng, *J. Am. Chem. Soc.* 142 (2020) 12613–12619.
- [62] S. Kar, M. Rauch, G. Leitius, Y. Ben-David, D. Milstein, *Nat. Catal.* 4 (2021) 193–201.
- [63] Z. Wang, S. Wang, L. Ma, Y. Guo, J. Sun, N. Zhang, R. Jiang, *Small* 17 (2021), 2006770.
- [64] Y.C. Dong, P.P. Lopes, P. Martins, H. He, T. Kawaguchi, P. Zapol, H. You, D. Tripkovic, D. Strmcnik, Y. Zhu, S. Seifert, S. Lee, V. Stamenkovic, N. Markovic, *Nat. Energy* 5 (2020) 550.
- [65] X. Liang, L. Shi, R. Cao, G. Wan, W. Yan, H. Chen, Y. Liu, X. Zou, *Adv. Mater.* 32 (2020), 2001430.
- [66] M. Wang, L. Zhang, Y. He, H. Zhu, *J. Mater. Chem. A* 9 (2021) 5320–5363.
- [67] H. Liao, T. Luo, P. Tan, K. Chen, L. Lu, Y. Liu, M. Liu, J. Pan, *Adv. Funct. Mater.* (2021), 2102772.
- [68] R. Gao, D. Yan, *Adv. Energy Mater.* 10 (2019), 1900954.
- [69] J. Jeong, Soo-Kil, S. Ki, B. Keun, *Appl. Catal. B-Environ.* 237 (2018) 409–415.

- [70] C. Liu, D. Jia, Q. Hao, X. Zheng, Y. Li, C. Tang, H. Liu, J. Zhang, X. Zheng, *ACS Appl. Mater. Interfaces* 11 (2019) 27667–27676.
- [71] X. Luo, P. Ji, P. Wang, R. Cheng, D. Chen, C. Lin, J. Zhang, J. He, Z. Shi, N. Li, S. Xiao, S. Mu, *Adv. Energy Mater.* 10 (2020), 1903891.
- [72] B. Li, Z. Li, Q. Pang, J.Z. Zhang, *Chem. Eng. J.* 401 (2020), 126045.
- [73] C. Liu, T. Gong, J. Zhang, X. Zheng, J. Mao, H. Liu, Y. Li, Q. Hao, *Appl. Catal. B-Environ.* 262 (2019), 118245.
- [74] R.V. Mom, J.N. Louwen, J.W.M. Frenken, I.M.N. Groot, *Nat. Commun.* 10 (2019) 2546.
- [75] K. Xu, P. Chen, X. Li, Y. Tong, H. Ding, X. Wu, W. Chu, Z. Peng, C. Wu, Y. Xie, *J. Am. Chem. Soc.* 137 (2015) 4119–4125.
- [76] J. Zhang, X. Shang, H. Ren, J. Chi, H. Fu, B. Dong, C. Liu, Y. Chai, *Adv. Mater.* 31 (2019), 190510731.
- [77] C. Liu, Y. Han, L. Yao, L. Liang, J. He, Q. Hao, J. Zhang, Y. Li, H. Liu, *Small* 17 (2021), 2007334.
- [78] P. Chen, T. Zhou, M. Zhang, Y. Tong, C. Zhong, N. Zhang, L. Zhang, C. Wu, Y. Xie, *Adv. Mater.* 29 (2017) 1701584.